Estimating Small-Body Gravity Field from Shape Model and Navigation Data

Ryan S. Park,* Robert A. Werner,† and Shyam Bhaskaran‡

Jet Propulsion Laboratory, California Institute of Technology, Pasadena, California, 91109

This paper presents a method to model the external gravitational field and to estimate the internal density variation of a small body. The first problem discussed is the modeling of the external gravitational field using finite element definitions, such as cubes and spheres, assuming the polyhedral shape and internal density distribution are provided. The gravitational attractions computed using finite element approach are compared with the true uniform-density polyhedral attraction and the level of accuracies are presented. The second problem discussed is the inverse problem where the internal density variation is determined by estimating the density of each finite element assuming the body shape, radiometric measurements, and a priori density constraints are given. This is presented via covariance analysis, which gives the level of uncertainty in the estimated densities. The result shows that the accuracy of the estimated density variation can be significantly improved depending on the orbit altitude, finite element resolution, and measurement accuracy, which indicates that the finite element approach can be used as a close-proximity navigation model around small bodies.

Nomenclature

$\mathbf{A}$	=	Jacobian matrix
e_{12}	=	edge length
G	=	universal gravitational constant, 6.67428×10^{-8} cm^3/g/s^2
$\mathbf{h}_R, \mathbf{h}_D$	=	instantaneous range and range-rate measurement partials, respectively
$\mathcal{J}$	=	Jacobi constant
N	=	number of measurements
$\hat{\mathbf{n}}_f, \hat{\mathbf{n}}_A, \hat{\mathbf{n}}_B$	=	face normal vectors
$\hat{\mathbf{n}}_{12}^A, \hat{\mathbf{n}}_{21}^B$	=	edge normal vectors
$\mathbf{P}_0, \mathbf{P}_0^+$	=	epoch-state and updated epoch-state covariance matrices, respectively
p	=	Gaussian probability density function
$\mathbf{p}$	=	estimated density vector
$\mathbf{R}_0$	=	epoch-state square-root information filter matrix
$\mathbf{r}$	=	field-point position vector
$\mathbf{r}_{e1}, \mathbf{r}_{e2}$	=	vectors from a field point to vertices of an edge
$\mathbf{r}_f$	=	vector from a field point to some fixed point in the face plane
$\mathbf{r}_i, r_{mi}$	=	position vector and the radius of an ith sphere, respectively
$\mathbf{r}_s$	=	station location vector
$\mathbf{r}_0$	=	initial spacecraft position vector
S_n	=	face vertex angle viewed from $\mathbf{r}$
U_p, U_c, U_m	=	gravitational potentials of a polyhedral shape, finite cube shape, and finite sphere shape models, respectively
$\mathbf{v}_0$	=	initial spacecraft velocity vector
$\mathbf{W}$	=	measurement weight matrix
$\mathbf{x}_0, \mathbf{x}_a$	=	estimated and a priori epoch-state vectors, respectively
$\mathbf{z}^*, \mathbf{z}$	=	actual (i.e., observed data) and predicted measurement vectors, respectively
$\tilde{\mathbf{z}}$	=	data vector
z_R, z_D	=	instantaneous range and range-rate measurements, respectively
δ_{ij}	=	Kronecker delta function
$\boldsymbol{\Lambda}_a, \boldsymbol{\Lambda}_0$	=	a priori and epoch-state information matrices, respectively
$\boldsymbol{\Lambda}_0^+$	=	updated epoch-state information matrix
λ_{ij}	=	percent difference between the attractions from model i and model j
$\boldsymbol{\rho}$	=	station-to-spacecraft vector
ϱ	=	density (g/cm^3)
ϱ_i	=	density of an ith finite element (g/cm^3)
σ_k	=	noise of the kth measurement
$\boldsymbol{\Phi}_k$	=	$\boldsymbol{\Phi}(t_k, t_0)$, state transition matrix mapping the deviation from t_0 to t_k
ω_f	=	face projected area
∇	=	gradient operator

*Member of Engineering Staff, Outer Planet Navigation Group; ryan.s.park@jpl.nasa.gov. Senior Member AIAA.

†Senior Member of Engineering Staff, Optical Navigation Group; robert.a.werner@jpl.nasa.gov.

‡Group Supervisor, Outer Planet Navigation Group; shyam.bhaskaran@jpl.nasa.gov. Member AIAA.

I. Introduction

OVER the past decade, there has been a growing interest in exploring small bodies (i.e., asteroids, comets, and planetary satellites). To name a few, missions such as NEAR (1996), Deep Space 1 (1998), Stardust (1999), MUSES-C (2002), Rosetta (2004), Deep Impact (2005), and Dawn (2007) have visited or will visit small bodies, where their mission objectives range from orbiting and flyby to landing on the surface. Among many critical requirements of such missions, one of the most crucial components is an accurate characterization of the spacecraft orbit environment as it is usually directly related to the quality of science outcome. In general, small bodies have irregular shapes as their local gravity is not strong enough to pull the body into a spherical shape, and thus, accurately modeling its gravitational field is an extremely challenging astrodynamics problem.

The first problem discussed in this paper is the modeling of the external gravitational field using finite element definitions, such as cubes and spheres, assuming an accurate shape model and internal density variation of a small body are provided. Conventionally, there are two fundamentally different ways of modeling the external

gravitational field of a small body [1]. The first approach is the use of a series expansion to approximate the gravitational potential, such as using external spherical harmonics [2]. For example, Garmier and Barriot [3] discuss how to model the gravity potential using external ellipsoidal harmonics. When the body in question is close to a sphere (e.g., planets) and when the field point is outside the Brillouin sphere (i.e., the minimum sphere which circumscribes the body), spherical harmonics can provide a very good approximation of the overall gravitational field. When the field point is inside the Brillouin sphere, however, these series diverge in general, which makes the use of spherical harmonics not suitable especially for irregularly shaped bodies. The second approach is the direct computation of the gravitational potential using a finite number of polyhedral definitions [4,5]. This approach, however, usually assumes that the body has a constant density, and thus, it may not be a good model for a body with significant density variation. It is possible to subdivide a polyhedron into multiple polyhedrons, but such an algorithm for subdivision is not trivial and our proposed method is, in a sense, the simplest and natural extension of a kind.

Because this paper focuses on an irregularly shaped small body with significant density variation, the external spherical harmonics or the constant-density polyhedron may not be sufficient to accurately approximate the true gravity field. An interesting work is discussed in Scheeres et al. [6], where an irregularly shaped body is divided into multiple constant-density tetrahedrons and a least-squares approach is applied to estimate the density of each tetrahedron given predetermined spherical harmonics. As an alternate method, this paper proposes a finite element based approach and presents the corresponding gravitational potential and necessary derivatives. A high-precision polyhedral shape model is assumed to be available from an optical survey, and based on this shape model, the body interior is filled up with finite elements such as cubes (i.e., regular hexahedrons) or spheres with distinct density values. For example, Fig. 1a is a predicted shape model of Itokawa from a radar survey before MUSES-C arrival and Figs. 1b and 1c illustrate how a shape model can be constructed using finite cubes and spheres, respectively. Once a physical finite element shape model is available, it is straight forward to compute the attraction whether a spacecraft is inside a Brillouin sphere or the body has a strong density variation. The gravitational attractions based on finite element shape models are compared with the true attraction from a polyhedron model and the level of accuracy is discussed.

The second problem discussed is the inverse problem where the internal density variation is determined by estimating the density of each finite element, assuming that the body shape, radiometric measurements, and a priori density constraints are given. In practice, the inverse problem is much more difficult than the modeling problem because it is generally an ill-conditioned problem depending on the order of accuracy of the density variation one is solving for. In other words, the sensitivity due to each finite element becomes indistinguishable when the element size becomes too small. As an example, we discuss how well the density variation can be estimated based on the polyhedral shape model shown in Fig. 1a with different finite element resolution, orbit altitude, and measurement accuracy. This is presented via covariance analysis, which gives the level of uncertainty in the estimated densities. The advantage of the proposed finite element approach is that the measurements taken inside the Brillouin sphere can be used. Moreover, the estimated

density of each finite element has a physical meaning, whereas it is not trivial to apprehend the physical meaning of spherical harmonics.

II. Gravitational Potential of a Small Body

The following section presents the governing equations used in computing the gravitational potentials of constant-density polyhedron and finite element shape models. The modeling accuracy of different shape models by comparing the gravitational attractions is also discussed.

A. Potential of a Constant-Density Polyhedron

Following the notations used in Werner [4], the gravitational potential of a polyhedral body at a field point $\mathbf{r}$ can be represented as

$$U_p(\mathbf{r}) = \frac{1}{2}G\varrho \sum_{e\in\text{edges}} \mathbf{r}_e^T \mathbf{E}_e \mathbf{r}_e \cdot L_e - \frac{1}{2}G\varrho \sum_{f\in\text{faces}} \mathbf{r}_f^T \mathbf{F}_f \mathbf{r}_f \cdot \omega_f \quad (1)$$

where

$$\mathbf{r}_e = \mathbf{r}_{e1} - \mathbf{r} \quad (2)$$

$$\mathbf{E}_e = \hat{\mathbf{n}}_A(\hat{\mathbf{n}}_{12}^A)^T + \hat{\mathbf{n}}_B(\hat{\mathbf{n}}_{21}^B)^T \quad (3)$$

$$L_e = \ell_n \frac{r_{e1} + r_{e2} + e_{12}}{r_{e1} + r_{e2} - e_{12}} \quad (4)$$
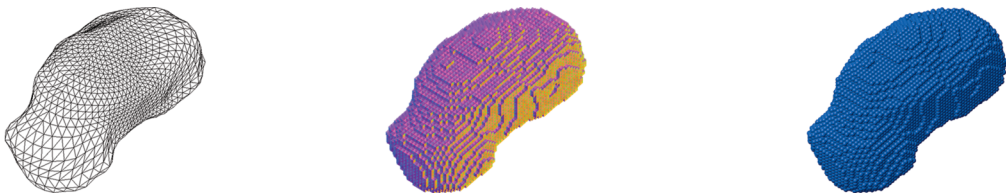
$$\mathbf{r}_f = \mathbf{r}_{f1} - \mathbf{r} \quad (5)$$

$$\mathbf{F}_f = \hat{\mathbf{n}}_f \hat{\mathbf{n}}_f^T \quad (6)$$

$$\omega_f = \begin{cases} 2\arctan\frac{D_f - \text{run}|\omega_f|}{\text{rise}|\omega_f|}, & z > 0 \\ 0, & z = 0 \\ 2\arctan\frac{\text{run}|\omega_f| - D_f}{-\text{rise}|\omega_f|}, & z < 0 \end{cases} \quad (7)$$

$$D_f = \sqrt{(\text{run}|\omega_f|)^2 + (\overline{\text{rise}|\omega_f|})^2} \quad (8)$$

$$\begin{bmatrix} \text{run}|\omega_f| \\ \overline{\text{rise}|\omega_f|} \end{bmatrix} = \begin{bmatrix} -\text{run}S_n & \overline{\text{rise}S_n} \\ -\overline{\text{rise}S_n} & -\text{run}S_n \end{bmatrix} \cdots \begin{bmatrix} -\text{run}S_2 & \overline{\text{rise}S_2} \\ -\overline{\text{rise}S_2} & -\text{run}S_2 \end{bmatrix}$$
$$\times \begin{bmatrix} -\text{run}S_1 & \overline{\text{rise}S_1} \\ -\overline{\text{rise}S_1} & -\text{run}S_1 \end{bmatrix}\begin{bmatrix} 1 \\ 0 \end{bmatrix} \quad (9)$$

a) Polyhedron model (3688 faces) b) Finite-cube shape model (26311 elements) c) Finite-sphere shape model (26311 elements)
Fig. 1 Different types of a small-body shape model.

$$\text{run } S_j = (\mathbf{r}_i^T \mathbf{r}_k) r_j^2 - (\mathbf{r}_i^T \mathbf{r}_j)(\mathbf{r}_j^T \mathbf{r}_k) \qquad (10)$$

$$\overline{\text{rise} S_j} = \mathbf{r}_i \cdot (\mathbf{r}_j \times \mathbf{r}_k) \cdot r_j \qquad (11)$$

From the potential function, the acceleration, gravity-gradient matrix, and Laplacian at a field point $\mathbf{r}$ can be derived as

$$\frac{\partial U_p}{\partial \mathbf{r}} = -G\varrho \sum_{e \in \text{edges}} \mathbf{E}_e \mathbf{r}_e \cdot L_e + G\varrho \sum_{f \in \text{faces}} \mathbf{F}_f \mathbf{r}_f \cdot \omega_f \qquad (12)$$

$$\frac{\partial^2 U_p}{\partial \mathbf{r}^2} = G\varrho \sum_{e \in \text{edges}} \mathbf{E}_e \cdot L_e - G\varrho \sum_{f \in \text{faces}} \mathbf{F}_f \cdot \omega_f \qquad (13)$$

$$\nabla^2 U_p = -G\varrho \sum_{f \in \text{faces}} \omega_f \qquad (14)$$

Note that computing the Laplacian gives whether a field point is inside, outside, on a face, or on a vertex or an edge:

$$-\frac{\nabla^2 U_p(\mathbf{r}_i)}{G\varrho} = \begin{cases} 4\pi, & \text{if inside} \\ 0, & \text{if outside} \\ 2\pi, & \text{if on a face} \\ \text{solid angle}, & \text{if on a vertex or an edge} \end{cases} \qquad (15)$$

B. Potential of Multiple Finite Cube and Finite Sphere Shape Models

To create a finite cube shape model from a polyhedral body, a rectangular box that circumscribes the entire body is first determined. The rectangular box is then meshed with a predefined cube length ℓ and the Laplacian of each grid point is checked. The grid point is stored only if it is inside the body or on the surface. This way, multiple cubes with physical length ℓ can be obtained where their center points lie inside the body or on the surface. Note that this method does not perfectly model the surface variation as some cubes will have excess volumes and some polyhedron spaces will not be covered. The most trivial way to resolve this problem would be to decrease ℓ, because in limit $\ell \to 0$, $U_c \to U_p$, where U_c is the potential of the finite cube shape model. This approach, however, increases the computational cost tremendously and, as we will see later, estimating the density variation may become an ill-conditioned problem depending on the cube size.

Another direct way to resolve surface variation problem would be to completely cover the entire polyhedron using cubes such that there are no empty spaces left and to reshape the surface-intersecting cubes as parallelepipeds, tetrahedrons, or even general polyhedrons so that the polyhedron surface can be approximated more accurately. An indirect, yet simpler, way would be to apply density that is proportional to the volume difference to the surface-intersecting cubes. (This density correction method can also be applied to a finite sphere shape model as well.) These approaches would yield physically more accurate shape representations, but are not considered in this study.

Given multiple cubes, it is straight forward to come up with the following gravitational potential function and related derivatives at a field point $\mathbf{r}$:

$$U_c(\mathbf{r}) = \sum_{i \in \text{cubes}} \left(\frac{1}{2} G\varrho_i \sum_{e \in \text{edges}} \mathbf{r}_e^T \mathbf{E}_e \mathbf{r}_e \cdot L_e - \frac{1}{2} G\varrho_i \sum_{f \in \text{faces}} \mathbf{r}_f^T \mathbf{F}_f \mathbf{r}_f \cdot \omega_f \right) \qquad (16)$$

$$\frac{\partial U_c}{\partial \mathbf{r}} = \sum_{i \in \text{cubes}} \left(-G\varrho_i \sum_{e \in \text{edges}} \mathbf{E}_e \mathbf{r}_e \cdot L_e + G\varrho_i \sum_{f \in \text{faces}} \mathbf{F}_f \mathbf{r}_f \cdot \omega_f \right) \qquad (17)$$

$$\frac{\partial^2 U_c}{\partial \mathbf{r}^2} = \sum_{i \in \text{cubes}} \left(G\varrho_i \sum_{e \in \text{edges}} \mathbf{E}_e \cdot L_e - G\varrho_i \sum_{f \in \text{faces}} \mathbf{F}_f \cdot \omega_f \right) \qquad (18)$$

$$\frac{\partial}{\partial \varrho_j} \left(\frac{\partial U_c}{\partial \mathbf{r}} \right) = \sum_{i \in \text{cubes}} \left(-G\delta_{ij} \sum_{e \in \text{edges}} \mathbf{E}_e \mathbf{r}_e \cdot L_e + G\delta_{ij} \sum_{f \in \text{faces}} \mathbf{F}_f \mathbf{r}_f \cdot \omega_f \right) \qquad (19)$$

If finite spheres are used (i.e., point masses), the corresponding gravitational potential, acceleration, gravity-gradient matrix, and partial of acceleration with respect to density are

$$U_m(\mathbf{r}) = \sum_{i \in \text{spheres}} \frac{4\pi}{3} r_{mi}^3 G\varrho_i \frac{1}{\|\mathbf{r} - \mathbf{r}_i\|} \qquad (20)$$

$$\frac{\partial U_m}{\partial \mathbf{r}} = \sum_{i \in \text{spheres}} -\frac{4\pi}{3} r_{mi}^3 G\varrho_i \frac{\mathbf{r} - \mathbf{r}_i}{\|\mathbf{r} - \mathbf{r}_i\|^3} \qquad (21)$$

$$\frac{\partial^2 U_m}{\partial \mathbf{r}^2} = \sum_{i \in \text{spheres}} \frac{4\pi}{3} r_{mi}^3 G\varrho_i \frac{1}{\|\mathbf{r} - \mathbf{r}_i\|^5} \left[\mathbf{I}_{3 \times 3} - 3 \frac{(\mathbf{r} - \mathbf{r}_i)(\mathbf{r} - \mathbf{r}_i)^T}{\|\mathbf{r} - \mathbf{r}_i\|^2} \right] \qquad (22)$$

$$\frac{\partial}{\partial \varrho_j} \left(\frac{\partial U_m}{\partial \mathbf{r}} \right) = -\frac{4\pi}{3} r_{mj}^3 G \frac{\mathbf{r} - \mathbf{r}_j}{\|\mathbf{r} - \mathbf{r}_j\|^3} \qquad (23)$$

where $\mathbf{r}_i$ and r_{mi} represent the sphere center vector and the radius of an ith sphere, respectively. Note that a finite cube can always be modeled using finite spheres because the size of spheres can always be reduced to fill up the cube. This approach, as discussed earlier in this section, would increase the computational cost and estimating the density variation may become an ill-conditioned problem.

C. Comparison of the Attractions of a Finite Cube and a Finite Sphere

Consider a cube with length ℓ. Assuming a sphere has the same density and mass as the cube, its corresponding radius is $r_m = (3/4\pi)^{1/3} \ell \approx 0.62\ell$. The masses should be the same because the point-mass approximations of both shapes should be identical. Now define λ_{ij} as follows:
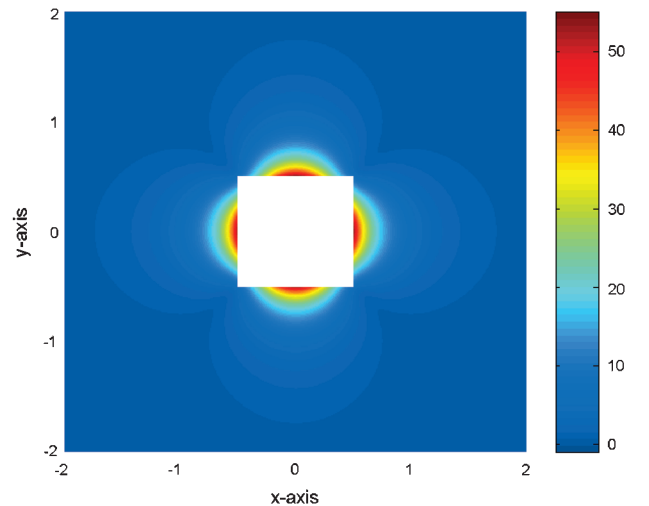

Fig. 2 Percent difference between the attractions from a finite cube and a finite sphere.

a) Along x-y plane

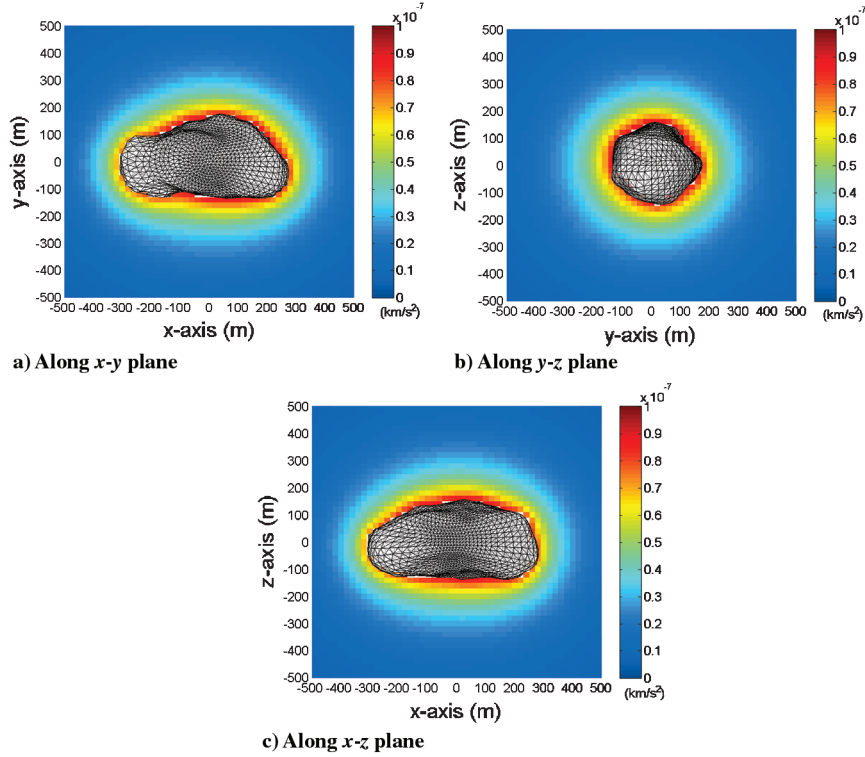b) Along y-z plane

c) Along x-z plane

Fig. 3   Attraction magnitude of a 20 m finite cube shape model.

$$\lambda_{ij} = \frac{\|\partial U_i / \partial \mathbf{r} - \partial U_j / \partial \mathbf{r}\|}{\|\partial U_i / \partial \mathbf{r}\|} \times 100\% \qquad (24)$$

which represents the percent difference between the attractions from the model i and model j; for example, λ_{cm} represents the percent difference between finite cube and finite sphere shape models. Assuming a unit cube, Fig. 2 shows λ_{cm} along the x–y plane, which is also discussed in the work of Werner and Scheeres [5]. Because the masses are the same, in limit ($\|\mathbf{r}\| \rightarrow \infty$), $\lambda_{cm} \rightarrow 0\%$. Note that, in general, the difference is very small ($\lambda_{cm} < 0.5\%$) when the field point is about 2ℓ distance away from the center. The maximums occur on the surfaces ($\lambda_{cm} \approx 54\%$). This indicates that, depending on the location of the field point, a cube can be approximated as a sphere, which is generally easier to implement and computationally faster.

D.   Comparison of the Attractions of Finite Cube, Finite Sphere, and Polyhedral Shape Models

Consider the Itokawa polyhedral shape model shown in Fig. 1a, which has 1846 vertices and 3688 faces. In this study, the polyhedron density is assumed to be constant [7] (1.9 g/cm³) and the corresponding volume is [8]

$$\sum_{i \in \text{faces}} \frac{\det[\mathbf{r}_{i1}, \mathbf{r}_{i2}, \mathbf{r}_{i3}]}{6} = 0.026278 \text{ km}^3 \qquad (25)$$

where $\mathbf{r}_{ij}$ is the jth vertex position vector of the ith face. The polyhedral shape is modeled using finite elements based on the method discussed in Sec. II.B. Assuming a 20-m-resolution finite cube shape model, 3292 cubes are used, and in order to keep total mass the same, the density of each cube is corrected to $M_{\text{Itokawa}}/V_{\text{total cubes}} = 1.896$ g/cm³, where $V_{\text{total cubes}} = 0.026336$ km³. The finite sphere shape model is obtained in a similar manner where each sphere has the corresponding radius of 12.41 m. (Both cube and sphere are assumed to have the same density, mass, and volume, and thus, the only difference is their physical shapes.)

Figures 3a–3c show the attractions (i.e., $\partial U_c / \partial \mathbf{r}$) based on a 20 m finite cube shape model along different sections. As expected, irregular gravitational attraction near the surface is observed and becomes more concentrically distributed as the field point moves

away from the center. Figures 4a, 4c, and 4e show λ_{pc}, which represents the percent difference in the attractions between the polyhedral and finite cube shape models. A poor agreement is observed near the surface, which is mostly because the surface variation is not modeled as discussed in Sec. II.B. Figures 4b, 4d, and 4f show λ_{cm}, and as expected, a very good agreement is observed except for the points near the surface, which is essentially the result discussed in Sec. II.C.

III.   Covariance Analysis

So far, the modeling of the gravitational field of a small body is discussed. The following two sections present the inverse problem, which show how well the internal density variation of a small body can be determined by estimating the density of each finite element. In this section, a batch least-squares filter formulation is reviewed and the importance of covariance analysis is discussed. Moreover, to retain numerical precision, implementation of square-root information filter (SRIF) technique is presented.

A.   Batch Least-Squares Filter

Define the cost function J as follows[§]:

$$J(\mathbf{x}_0) = \frac{1}{2}(\mathbf{x}_0 - \mathbf{x}_a)^T \mathbf{\Lambda}_a (\mathbf{x}_0 - \mathbf{x}_a) + \frac{1}{2}[\mathbf{z}^* - \mathbf{z}(\mathbf{x}_0)]^T \mathbf{W}[\mathbf{z}^* - \mathbf{z}(\mathbf{x}_0)] \qquad (26)$$

Under ideal conditions (i.e., perfect dynamic model and observables), the cost function J should vanish to zero for each $\mathbf{x}_0$. In practice, however, errors always exist in both the dynamics and measurement models. The goal of the batch least-squares filter is to find the initial state $\mathbf{x}_0$ such that the cost function J is minimized given $\mathbf{z}^*$.

By applying the necessary conditions to Eq. (26) and by linearizing about the nominal motion, $\bar{\mathbf{x}}_0$, the following normal equation is obtained:

[§]Note that $\mathbf{x}_0$ is not necessarily limited to the spacecraft initial state vector. It can be augmented to include any parameters of interest, such as dynamics and measurement biases.

a) Along x-y plane (λ_{pc})   b) Along x-y plane (λ_{cm})

c) Along y-z plane (λ_{pc})   d) Along y-z plane (λ_{cm})

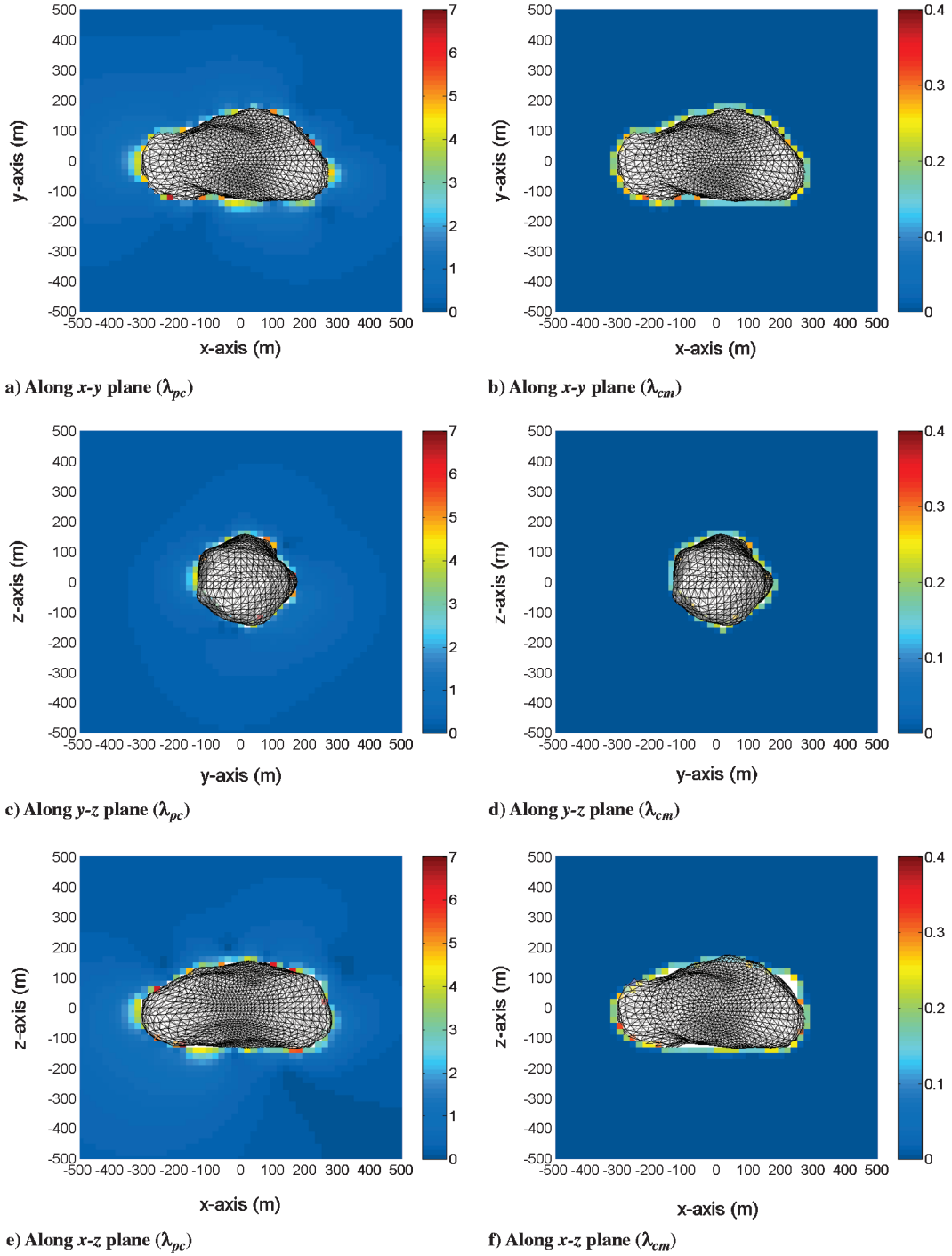e) Along x-z plane (λ_{pc})   f) Along x-z plane (λ_{cm})

Fig. 4 Comparison of the attraction magnitudes from polyhedral, finite cube (20 m length), and finite sphere (12.41 m radius) shape models. The figures on the left show λ_{pc} and the figures on the a right show λ_{cm} along different sections.

$$\underbrace{[\mathbf{\Lambda}_a + \mathbf{H}_{\mathbf{x}_0}^T \mathbf{W} \mathbf{H}_{\mathbf{x}_0}]}_{\mathbf{\Lambda}_0} \delta\mathbf{x}_0 = \underbrace{\mathbf{\Lambda}_a \delta\mathbf{x}_a + \mathbf{H}_{\mathbf{x}_0}^T \mathbf{W} \Delta\mathbf{z}}_{\tilde{\mathbf{z}}}, \qquad \mathbf{\Lambda}_0 \delta\mathbf{x}_0 = \tilde{\mathbf{z}}$$

(27)

where $\delta\mathbf{x}_a = \mathbf{x}_a - \bar{\mathbf{x}}_0$, $\Delta\mathbf{z} = \mathbf{z}^* - \mathbf{z}(\bar{\mathbf{x}}_0)$, and

$$\mathbf{H}_{\mathbf{x}_0} = \frac{\partial \mathbf{z}}{\partial \mathbf{x}_0}\bigg|_{\mathbf{x}_0=\bar{\mathbf{x}}_0} = \begin{bmatrix} \mathbf{h}_1 \mathbf{\Phi}_1 \\ \vdots \\ \mathbf{h}_N \mathbf{\Phi}_N \end{bmatrix}$$

(28)

The differential equations of the state transition matrix (STM) are defined as

$$\dot{\mathbf{\Phi}} = \frac{\partial}{\partial\mathbf{x}}\left(\frac{d\mathbf{x}}{dt}\right)\mathbf{\Phi} = \mathbf{A}\mathbf{\Phi}$$

(29)

In summation notation, the epoch-state information matrix and the data vector can be stated as

$$\mathbf{\Lambda}_0 = \mathbf{\Lambda}_a + \sum_{k=1}^{N} \frac{1}{\sigma_k^2} \mathbf{\Phi}_k^T \mathbf{h}_k^T \mathbf{h}_k \mathbf{\Phi}_k$$

(30)

$$\tilde{\mathbf{z}} = \mathbf{\Lambda}_a \delta\mathbf{x}_a + \sum_{k=1}^{N} \frac{1}{\sigma_k^2} \mathbf{\Phi}_k^T \mathbf{h}_k^T [\mathbf{z}_k^* - \mathbf{z}_k(\bar{\mathbf{x}}_0)]$$

(31)

Once the epoch-state information matrix is computed, the epoch-state covariance matrix can be obtained by computing $\mathbf{P}_0 = \mathbf{\Lambda}_0^{-1}$.

The least-squares filter computes the correction vector $\delta \mathbf{x}_0$ and iterates until the solution converges, which usually depends on some user-defined quantities (e.g., $\|\delta \mathbf{x}_0\| < \epsilon_{\delta \mathbf{x}_0}$) [9,10]. When carrying out a batch least-squares covariance analysis, however, one is only interested in computing $\mathbf{\Lambda}_0$ as it conveys how well the estimations of the estimate vector $\mathbf{x}_0$ can be made by processing N measurements. To see this, let each measurement have Gaussian statistics so that each residual can be represented as $\epsilon = \mathbf{z}^* - \mathbf{z}(\mathbf{x}_0) \sim \mathcal{N}(\mathbf{0}, \mathbf{W}^{-1})$, which is a usual assumption made in conventional trajectory navigation. Given the statistical properties of the processed measurements, the goal is to characterize the statistics of the estimate vector $\mathbf{x}_0$. Computing the first two central moments results in

$$E[\mathbf{x}_0^{\text{lsq}}] = E[\bar{\mathbf{x}}_0 + \delta \mathbf{x}_0] = \mathbf{x}_0 \qquad (32)$$

$$\mathbf{P}_0^{\text{lsq}} = E[(\mathbf{x}_0^{\text{lsq}} - E[\mathbf{x}_0^{\text{lsq}}])(\mathbf{x}_0^{\text{lsq}} - E[\mathbf{x}_0^{\text{lsq}}])^T] = (\mathbf{\Lambda}_a + \mathbf{H}_{\mathbf{x}_0}^T \mathbf{W} \mathbf{H}_{\mathbf{x}_0})^{-1} \qquad (33)$$

Therefore, the estimate vector $\mathbf{x}_0$ is indeed a Gaussian vector with $\mathbf{x}_0^{\text{lsq}} \sim \mathcal{N}(\mathbf{x}_0, \mathbf{\Lambda}_0^{-1})$, or the full Gaussian probability density function of $\mathbf{x}_0^{\text{lsq}}$ can be given as

$$p(\mathbf{x}_0^{\text{lsq}}) = \frac{\sqrt{\det \mathbf{\Lambda}_0}}{(2\pi)^{n/2}} \exp\left[-\frac{1}{2}(\mathbf{x}_0^{\text{lsq}} - \mathbf{x}_0)^T \mathbf{\Lambda}_0 (\mathbf{x}_0^{\text{lsq}} - \mathbf{x}_0)\right] \qquad (34)$$

$$Pr(\mathbf{x}_0^{\text{lsq}} \in \mathcal{B}) = \int_{\mathcal{B}} p(\mathbf{x}_0) \, d\mathbf{x}_0 \qquad (35)$$

Therefore, it is evident that the information matrix $\mathbf{\Lambda}_0$ characterizes the statistical properties of $\mathbf{x}_0$, and thus, the least-squares covariance analysis is a useful filter design tool. In this paper, a batch least-squares covariance analysis is presented rather than a full estimation simulation because the goal of this study is to analyze the level of expected accuracies of the estimated densities from processing radiometric measurements.

B. Square-Root Information Filter Measurement Update

It has been known for many years that numerical precision is often lost in the covariance computation due to numerical round-off and measurement update errors (i.e., matrix inversion). In the actual simulation, SRIF algorithm is implemented in order to retain numerical precision [9–11]. Define the epoch-state information matrix as

$$\mathbf{\Lambda}_0 = \mathbf{R}_0^T \mathbf{R}_0 \qquad (36)$$

where the epoch-state SRIF matrix $\mathbf{R}_0$ is updated at every measurement increment. When a measurement is updated at t_k,

$$\mathbf{\Lambda}_0^+ = \mathbf{R}_0^T \mathbf{R}_0 + \frac{1}{\sigma_k^2} \mathbf{\Phi}_k^T \mathbf{h}_k^T \mathbf{h}_k \mathbf{\Phi}_k = \begin{bmatrix} \mathbf{R}_0 \\ \dfrac{\mathbf{h}_k \mathbf{\Phi}_k}{\sigma_k} \end{bmatrix}^T \mathbf{T}_H^T \mathbf{T}_H \begin{bmatrix} \mathbf{R}_0 \\ \dfrac{\mathbf{h}_k \mathbf{\Phi}_k}{\sigma_k} \end{bmatrix}$$

$$= \begin{bmatrix} \mathbf{R}_H \\ \mathbf{0} \end{bmatrix}^T \begin{bmatrix} \mathbf{R}_H \\ \mathbf{0} \end{bmatrix} \qquad (37)$$

where $\mathbf{T}_H$ is an orthogonal Householder transformation matrix that satisfies $\mathbf{T}_H^T \mathbf{T}_H = \mathbf{I}$ and $\mathbf{R}_H$ is an upper triangular matrix that becomes the updated epoch-state SRIF matrix. In the actual computation, QR-factorization is adapted as the Householder transformation [12]. After the Householder transformation is applied, the updated epoch-state information matrix becomes

$$\mathbf{\Lambda}_0^+ = \mathbf{R}_H^T \mathbf{R}_H \qquad (38)$$

and the updated epoch-state covariance matrix yields

$$\mathbf{P}_0^+ = \mathbf{R}_H^{-1} \mathbf{R}_H^{-T} \qquad (39)$$

which represents the a posteriori uncertainty of the estimated initial state vector.

IV. Estimation of the Small-Body Density Distribution

This section presents the models and assumptions used in the full covariance analysis simulation and discusses the level of accuracy of the estimated density variation using finite element shape approaches. The fundamental limitation in decoupling the gravitational attraction from two point masses is first discussed and followed by the result of full covariance analysis based on a realistic small-body shape model.

A. Correlation Between Two Finite Spheres

Before carrying out a full covariance analysis, the correlation between the estimated densities based on a single measurement is analyzed. Consider two finite spheres located at $\mp \mathbf{c} = [\mp c, \ 0, \ 0]$ with volumes V_1 and V_2 and densities ϱ_1 and ϱ_2. The total attraction from two finite spheres is then

$$\mathbf{a} = -G\left(\varrho_1 V_1 \frac{\mathbf{r} + \mathbf{c}}{\|\mathbf{r} + \mathbf{c}\|^3} + \varrho_2 V_2 \frac{\mathbf{r} - \mathbf{c}}{\|\mathbf{r} - \mathbf{c}\|^3}\right) \qquad (40)$$

Now suppose the acceleration can be directly measured and the corresponding measurement partials can be computed; that is,

$$\mathbf{h} = \frac{\partial \mathbf{a}}{\partial(\varrho_1, \varrho_2)} = \left[-V_1 G\left(\frac{\mathbf{r} + \mathbf{c}}{\|\mathbf{r} + \mathbf{c}\|^3}\right), \ -V_2 G\left(\frac{\mathbf{r} - \mathbf{c}}{\|\mathbf{r} - \mathbf{c}\|^3}\right)\right] \qquad (41)$$

The epoch-state information matrix can be computed as $\mathbf{\Lambda}_0 = \mathbf{h}^T \mathbf{h}$, so that $\mathbf{P}_0 = \mathbf{\Lambda}_0^{-1}$. Figure 5 shows the correlation coefficient between finite sphere densities (i.e., $\mathbf{P}_{0,12}/\sqrt{\mathbf{P}_{0,11} \mathbf{P}_{0,22}}$), and note that both x and y axes are normalized by the radius c. [The x and y axes are normalized by the radius (c) so that two finite spheres are located at $(-1, 0)$ and $(1, 0)$.] Of interest is the correlation coefficient because it represents the measure of how much information content of a single acceleration measurement can be used to decouple the estimates of ϱ_1 and ϱ_2. Note that the correlation coefficient is invariant under the volume and density of finite spheres because only one measurement is taken at time zero. The result shows that the field point has to be at a close distance in order to obtain a meaningful measurement. Also, note that the information matrix is not invertible along the points $y = 0$, which is expected as the acceleration directions due to each finite sphere are parallel. The zero correlation occur when the field point to finite sphere vectors are perpendicular (i.e., the circle at the origin with radius c).
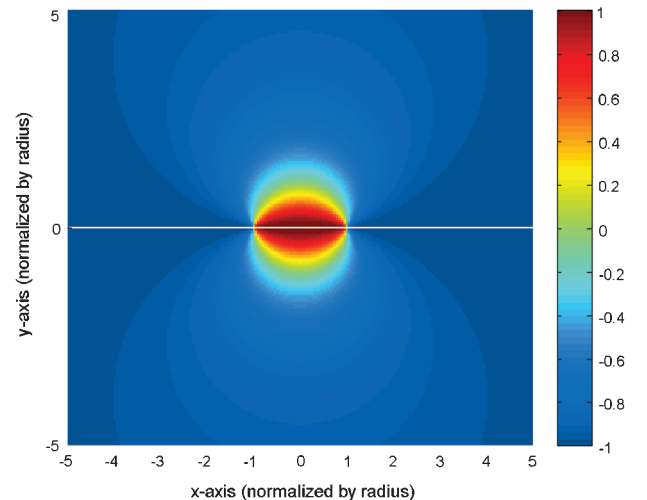

Fig. 5   Correlation of the estimated densities of two finite spheres.

Table 1   Initial conditions used in covariance analysis simulation

	Initial position, m	Initial velocity (m/s)	Initial orbit period, h
Case 1	$\mathbf{r}_0 = [-360, \quad 0, \quad 0]^T$	$\mathbf{v}_0 = [0, \quad -0.12026, \quad 0]^T$	22.6
Case 2	$\mathbf{r}_0 = [0, \quad 200, \quad 0]^T$	$\mathbf{v}_0 = [0.05, \quad 0, \quad 0.1188]^T$	2.69

Table 2   Orbit elements of the initial conditions used in covariance analysis simulation

	Semimajor axis, m	Eccentricity	Inclination, deg	Argument of periapsis, deg	Argument of ascending node, deg
Case 1	823	0.56	0.0	0.0	180
Case 2	199	0.0036	113	180	90

B. Estimated Uncertainties of Finite Cube and Finite Sphere Shape Models

In the full covariance analysis, the estimated variables are the initial spacecraft state and the density of each finite element; that is,

$$\mathbf{x} = [\mathbf{r}_0^T, \quad \mathbf{v}_0^T, \quad \mathbf{p}^T]^T \tag{42}$$

where

$$\mathbf{p} = [\varrho_1, \quad \cdots, \quad \varrho_M]^T \tag{43}$$

Note that ϱ_j represents the density of the jth element where $j \in \{1, \cdots, M\}$ depends on the number of elements in the finite element shape model. The equations of motion for the estimated vector are

$$\dot{\mathbf{x}} = \left[\mathbf{v}^T, \quad \frac{\partial U_i}{\partial \mathbf{r}}, \quad \mathbf{0}_{1 \times M}\right]^T \tag{44}$$

and the corresponding differential equations for the STM yield

$$\dot{\boldsymbol{\Phi}} = \begin{bmatrix} \mathbf{0}_{3 \times 3} & \mathbf{I}_{3 \times 3} & \mathbf{0}_{3 \times M} \\ \frac{\partial^2 U_i}{\partial \mathbf{r}^2} & \mathbf{0}_{3 \times 3} & \frac{\partial}{\partial \mathbf{p}}\left(\frac{\partial U_i}{\partial \mathbf{r}}\right) \\ \mathbf{0}_{M \times 3} & \mathbf{0}_{M \times 3} & \mathbf{0}_{M \times M} \end{bmatrix} \boldsymbol{\Phi} \tag{45}$$

where $i \in \{c, m\}$ for either a finite cube or a finite sphere shape model. In the actual computation, the integration of the STM of $\mathbf{p}$ is excluded because it is always an $M \times M$ identity matrix. Note that at each point of integration, the Jacobi constant ($\mathcal{J}$) is computed as a validation check[¶]; that is,

$$\mathcal{J} = \frac{1}{2}(\dot{x}^2 + \dot{y}^2 + \dot{z}^2) - U_i(x, y, z) \tag{46}$$

Our goal is to analyze how well the density vector $\mathbf{p}$ can be estimated by processing radiometric measurements. In this study, the first data type considered is the instantaneous range measurement[**]

$$z_R = \|\mathbf{r} - \mathbf{r}_s\| = \|\boldsymbol{\rho}\| \tag{47}$$

where $\mathbf{r}_s$ is the station location vector. Taking the partials of the range measurement with respect to the current state vector $\mathbf{x}$ yields [11,13]
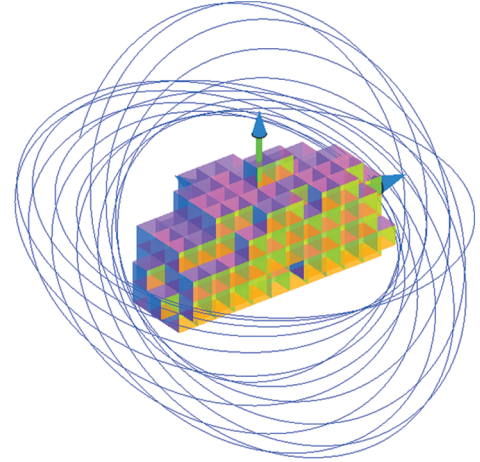
$$\mathbf{h}_R = \frac{\partial z_R}{\partial \mathbf{x}} = \left[\frac{\partial z_R}{\partial \mathbf{r}}, \quad \frac{\partial z_R}{\partial \mathbf{v}}, \quad \frac{\partial z_R}{\partial \mathbf{p}}\right] = [\hat{\boldsymbol{\rho}}^T, \quad \mathbf{0}_{1 \times 3}, \quad \mathbf{0}_{1 \times M}] \tag{48}$$

where $\hat{\boldsymbol{\rho}}$ is the unit tracking station-to-spacecraft position vector.

The second data type considered is the instantaneous range-rate measurement. (The information content of an instantaneous range-rate measurement is essentially the Doppler frequency shift in the transmitted signals.) Its analytic representation is

$$z_D = \frac{d}{dt}\|\mathbf{r} - \mathbf{r}_s\| = \hat{\boldsymbol{\rho}} \cdot \dot{\boldsymbol{\rho}} \tag{49}$$

a) 3-D trajectory and finite-cube shape model (211 elements)
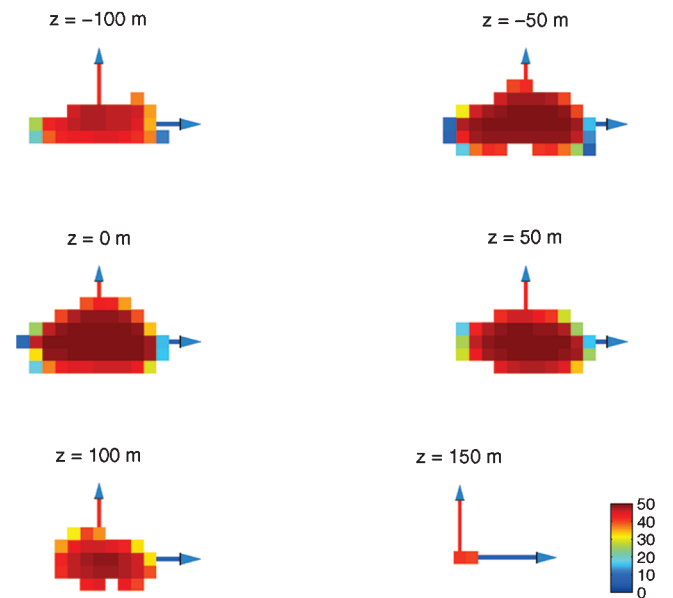
b) Density uncertainties along *x-y* cross sections (%)

Fig. 6   Case 1 trajectory based on 50 m cube resolution.

[¶]Because the gravity is a conservative force (i.e., energy is conserved) the Jacobi constant must be constant at all times.

[**]In practice, the instantaneous range measurements are modeled as the uplink and downlink signal travel times.

a) 3-D trajectory and finite-sphere shape model (211 elements)

z = -100 m   z = -50 m

z = 0 m   z = 50 m

z = 100 m   z = 150 m

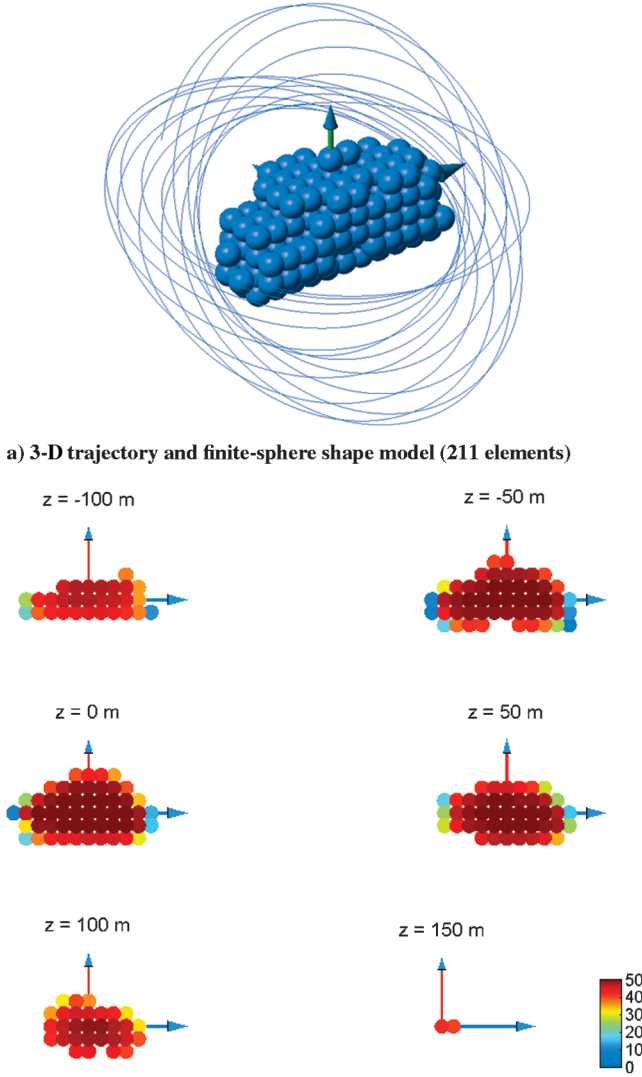b) Density uncertainties along *x-y* cross sections (%)

Fig. 7   Case 1 trajectory based on 31.02 m finite sphere radius.

Taking partials yields

$$\mathbf{h}_D = \frac{\partial z_D}{\partial \mathbf{x}} = \left[\dot{\boldsymbol{\rho}}^T \left(\frac{\partial \hat{\boldsymbol{\rho}}}{\partial \mathbf{r}} \right)^T, \quad \hat{\boldsymbol{\rho}}^T, \quad \mathbf{0}_{1 \times M} \right] \quad (50)$$

where

$$\frac{\partial \hat{\boldsymbol{\rho}}}{\partial \mathbf{r}} = \frac{1}{\rho} [\mathbf{I}_{3 \times 3} - \hat{\boldsymbol{\rho}} \hat{\boldsymbol{\rho}}^T] \quad (51)$$

Throughout this paper, the following assumptions are considered:

1) The central body is stationary.

2) Gravity is the only force acting on the spacecraft.

3) One tracking station is located at 2.5 km along the $+y$ axis. (Note that the tracking station is not located on Earth; however, it should not change the qualitative results shown in this paper since the overall information contents should be the same and the orbit geometry of a real mission can be modified to resemble this setup.)

4) There is no small-body occultation.

5) All trajectories are integrated for five days.

6) Both range and range-rate measurements are taken every 15 min.

7) Assuming X-band capability, the measurement accuracies are assumed to be 5 m and 0.075 mm/s for range and range-rate data, respectively [11].

8) The a priori covariance matrix is assumed to be diagonal with $(50 \text{ m})^2$, $(0.01 \text{ m/s})^2$, and $(50\%$ of the given density$)^2$ (i.e.,

0.946 g/m³ for 50 m or 0.948 g/m³ for 20 m finite cubes) for position, velocity, and density components, respectively.

9) Depending on the case, initial conditions are given in Table 1 and the corresponding orbit elements are shown in Table 2.

Figures 6a and 7a show the case 1 initial state integrated based on 50-m-resolution finite cube and finite sphere shape models, where the grid points are generated from the Itokawa shape model (i.e., Fig. 1a) using the method discussed in Sec. II.B. There are a total of 211 elements, the nominal density of 1.9 g/m³ is corrected to 1.893 g/m³ to preserve the same mass, and the corresponding finite sphere radius is 31.02 m. Figure 6b shows the a posteriori density uncertainties along sections defined by constant z planes of the shape model shown in Fig. 6a, where the green arrow represents the $+z$ axis. Recall that the a priori density uncertainties are 50 % for each element. As expected, only the cubes near the surface, where close flybys occur, have significant uncertainty improvement. The estimated root-sum-square of the a posteriori position uncertainties were ≈1 m and 0.25 mm/s for position and velocity, respectively. Figure 7b shows the same case based on a finite sphere shape and the same behavior is observed, as shown in Fig. 6b.

Figure 8a shows the case 1 initial state integrated based on a 20-m-resolution finite cube shape model, which corresponds to 3292 finite cubes. In this case, the nominal density is corrected to 1.896 g/m³. Figure 8b shows the estimated a posteriori density uncertainties of each 20-m-resolution finite cube and almost negligible change in the density uncertainties is observed when compared to the 50% a priori density uncertainty. This is mainly because the flyby distance is not close enough to decouple the measurement information content for each finite cube. This behavior is similar to a fundamental limit which exists when estimating the spherical harmonics from a spacecraft trajectory. Depending on the orbit altitude, there exists a limit on up to what degree and order spherical harmonic coefficients can be estimated [14]. One important item to note is that all the cases shown in Figs. 6–8 have the same level of mass uncertainties (∼0.1%). (The total mass uncertainty can be computed as

a) 3-D trajectory and finite-cube shape model (3292 elements)

z = –140 m   z = –120 m   z = –100 m   z = –80 m

z = –60 m   z = –40 m   z = –20 m   z = 0 m

z = 20 m   z = 40 m   z = 60 m   z = 80 m

z = 100 m   z = 120 m   z = 140 m

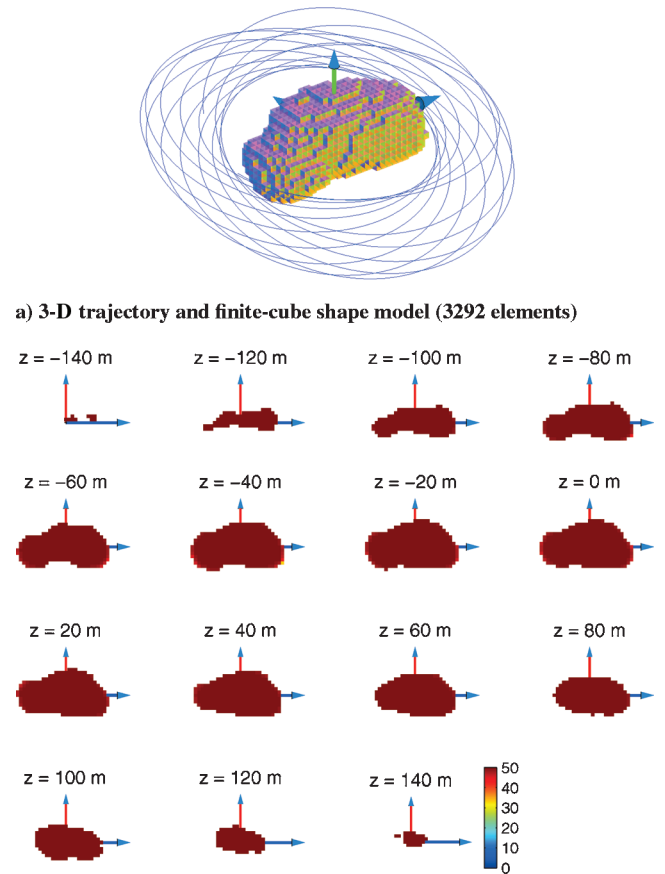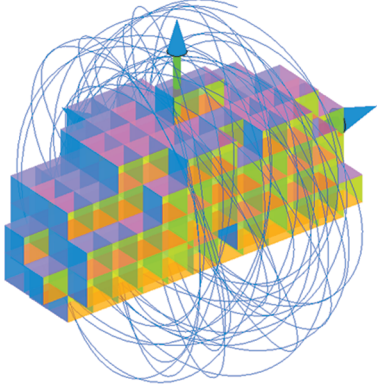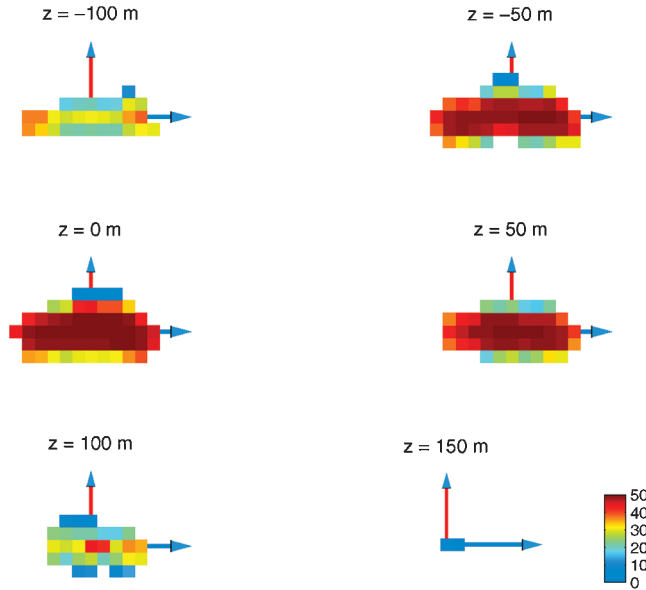b) Density uncertainties along *x-y* cross sections (%)

Fig. 8   Case 1 trajectory based on 20 m cube resolution.

a) 3-D trajectory and finite-cube shape model (211 elements)

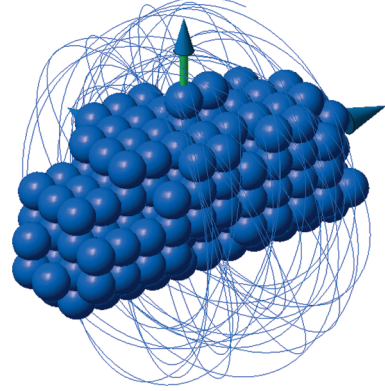b) Density uncertainties along *x-y* cross sections (%)

Fig. 9   Case 2 trajectory based on 50 m cube resolution.

a) 3-D trajectory and finite-sphere shape model (211 elements)

b) Density uncertainties along *x-y* cross sections (%)

Fig. 10   Case 2 trajectory based on 31.02 finite sphere radius assuming the measurement accuracy of 0.5 m and 0.0075 mm/s for range and range-rate data, respectively.

$$\sigma_{\text{total mass}} = \sqrt{\sum_i \sum_j v_i v_j \sigma_{\rho_i \rho_j}}$$

where v_i is the volume of an *i*th finite element and $\sigma_{\rho_i \rho_j}$ is the covariance of *i*th and *j*th density estimates.) In other words, the total information contents from the radiometric measurements are the same in all these cases, but very small improvement in the density uncertainty estimates is observed due to high correlations among the estimated density values.

Figures 9a and 10a show the case 2 initial state integrated based on 50-m-resolution finite cube and finite sphere shape models, respectively. Figure 9b shows the estimated uncertainties along the constant z planes. Improved uncertainty accuracies is observe which is mainly due to decreased orbit altitude. Although it is not shown here, modeling the body shape using finite spheres yields essentially the same result. Figure 10b shows the same case based on the corresponding finite sphere shape model and more accurate measurement accuracies of 0.5 m and 0.0075 mm/s for range and range-rate, respectively. When compared to Fig. 9b, significant improvement is observed, where the improvement ranges from factor of 1 to 6.2. A similar result is obtained when the body shape is modeled using finite cubes.

These results indicate that there exist sufficient information content to estimate the gravity field of a small body using a finite element approach, which is shown by the formal uncertainties in the estimated densities. For future studies, a full estimation simulation that recovers the true gravity field will be analyzed. In practice, a type of bootstrap method will probably be applied where the estimation process starts from large finite elements and refines as the orbit altitude is lowered. Another potential approach would be to estimate the spherical harmonics when the spacecraft is outside of the Brillouin sphere, and solve for the initial guess of the internal density values using a method such as discussed in Scheeres et al. [6].

V.   Conclusions

In this study, a finite element based approach to model the external gravitational field and to estimate the internal density variation of a small body is presented. Given a polyhedral shape model, the body interior was modeled using finite elements, such as cubes and spheres, and this paper showed that, depending on the finite element resolution and field-point distance from the small body, the finite element approach provides a very good approximation of the polyhedral gravity field. The main error comes from neglecting the surface variation and a number of potential ways to resolve this problem is discussed. Also, finite cube and finite sphere shape models showed noticeable difference only when the field point is very close to the surface.

The second problem presented is the covariance analysis of an inverse problem where a shape model, radiometric measurements, and a priori density constraints are given, and the internal density

variation is determined by estimating the density of each finite element. Based on covariance analysis, the result showed that the measurements taken inside the Brillouin sphere can be used and the accuracy of the estimated density uncertainties can be significantly improved depending on the finite element resolution, orbit altitude, and radiometric measurement accuracy. This indicates that the proposed finite element method is a good candidate for close-proximity navigation model around small bodies.

Acknowledgments

References

[1] Casotto, S., and Musotto, S., "Methods for Computing the Potential of an Irregular, Homogeneous, Solid Body and Its Gradient," Astrodynamics Specialist Conference, AIAA Paper 2000-4023, 2000.

[2] Kaula, W., *Theory of Satellite Geodesy Applications of Satellites to Geodesy*, Dover, New York, 2000, pp. 1–11.

[3] Garmier, R., and Barriot, J.-P., "Ellipsoidal Harmonic Expressions of the Gravitational Potential: Theory and Applications," *Celestial Mechanics and Dynamical Astronomy*, Vol. 79, No. 4, 2001, pp. 235–275.

[4] Werner, R., *On the Gravity Field of Irregularly Shaped Celestial Bodies*, Ph.D. Thesis, The University of Texas at Austin, Austin, TX, 1996.

[5] Werner, R., and Scheeres, D., "Exterior Gravitation of a Polyhedron Derived and Compared with Harmonic and Mascon Gravitation Representations of Asteroid 4769 Castalia," *Celestial Mechanics and Dynamical Astronomy*, Vol. 65, No. 3, 1997, pp. 313–344.

[6] Scheeres, D., Khushalani, B., and Werner, R., "Estimating Asteroid Density Distributions from Shape and Gravity Information," *Planetary and Space Science*, Vol. 48, No. 10, 2000, pp. 965–971.
doi:10.1016/S0032-0633(00)00064-7

[7] Fujiwara, A., Kawaguchi, J., Yeomans, D. K., Abe, M., Mukai, T., Okada, T., Saito, J., Yano, H., Yoshikawa, M., Scheeres, D. J., Barnouin-Jha, O., Cheng, A. F., Demura, H., Gaskell, R. W., Hirata, N., Ikeda, H., Kominato, T., Miyamoto, H., Nakamura, A. M., Nakamura, R., Sasaki, S., and Uesugi, K., "The Rubble-Pile Asteroid Itokawa as Observed by Hayabusa," *Science*, Vol. 312, No. 5778, 2006, pp. 1330–1334.
doi:10.1126/science.1125841

[8] Werner, R., "Spherical Harmonic Coefficients for the Potential of a Constant-Density Polyhedron," *Computers & Geosciences*, Vol. 23, No. 10, 1997, pp. 1071–1077.
doi:10.1016/S0098-3004(97)00110-6

[9] Bierman, G., *Factorization Methods for Discrete Sequential Estimation*, Vol. 128, Academic Press, New York, 1977, pp. 13–31.

[10] Crassidis, J., and Junkins, J., *Optimal Estimation of Dynamics Systems*, CRC Press, Boca Raton, FL, 2004, pp. 343–401.

[11] Park, R., Scheeres, D., Giampieri, G., Longuski, J., and Fischbach, E., "A Test of General Relativity: Estimating the Parameterized Post-Newtonian Parameters from Spacecraft Radiometric Measurements," *Journal of Spacecraft and Rockets*, Vol. 42, No. 3, 2005, pp. 559–568.
doi:10.2514/1.7647

[12] Montenbruck, O., and Gill, E., *Satellite Orbits*, 2nd ed., Springer, New York, 2001, pp. 268–272.

[13] Longuski, J., Fischbach, E., Scheeres, D., Giampieri, G., and Park, R., "Deflection of Spacecraft Trajectories as a New Test of General Relativity: Determining the PPN Parameters β and γ," *Physical Review D (Particles and Fields)*, Vol. 69, No. 042001, 2004, pp. 042001-1–042001-15.

[14] Konopliv, A., Miller, J., Owen, W., Yeomans, D., Giorgini, J., Garmier, R., and Barriot, J.-P., "A Global Solution for the Gravity Field, Rotation, Landmarks, and Ephemeris of Eros," *Icarus*, Vol. 160, No. 2, 2002, pp. 289–299.
doi:10.1006/icar.2002.6975